Improved Cohen-Sutherland algorithm for TGS transmission imaging

Yu-Cheng Yan[1,2,3] · Ming-Zhe Liu[1] · Xing-Yu Li[2] · Yu-Ting Xiong[2] · Yao Tan[4] · Zhuo Zuo[1,2,3] · Lan Chang[2,3] · Cui Li[2,3]

Abstract
Tomographic gamma scanner (TGS), an advanced γ-ray nondestructive analysis technique, can locate and analyze nuclides in radioactive nuclear waste, and TGS can be categorized into two processes: e.g., transmission measurement and emission measurement. Specifically, transmission measurements provide the basis for accurate measurement of nonuniform radionuclide content in TGS scanning. The scan data were obtained using the Monte Carlo tool Geant4 simulation, and 25 voxels were divided into five lengths and five widths in a square barrel. In this study, an encoding cropping algorithm based on draped foot vector judgment was adopted to rapidly calculate the voxel trace matrix within a square bucket of nuclear waste, and the transmission images were reconstructed using ordered subset expectation maximization. The results indicated that the cropping speed of the improved coding algorithm was significantly higher than that of the original algorithm, and the relative mean deviation and root-mean-square error between the reconstructed attenuation coefficient and the reference standard value tended to decrease with an increase in the cropped line segments in the voxel; the Pearson correlation coefficient tended to converge to 1.0. The image quality evaluation parameters of the high media-density materials were better than those of the low media-density materials in the above three indexes. The reconstruction effect was relatively poor for more complex filling materials. When there were more than 10 cropped line segments in the voxel, the reconstruction data generally tended to be stable. The graphical trimming algorithm can rapidly calculate the trace matrix of the scanned voxels; it exhibits the advantages of speed and efficiency and can serve as a novel method to solve the trace matrix of TGS nuclear waste transmission scans.

Keywords TGS · Cohen-Sutherland · Transmission scanning · Trace matrix

✉ Ming-Zhe Liu
liumz@cdut.edu.cn

1 State Key Laboratory of Geohazard Prevention and Geoenvironment Protection, Chengdu University of Technology, Chengdu 610059, China

2 The Engineering and Technical College of Chengdu University of Technology, Leshan 614000, China

3 Southwestern Institute of Physics, Chengdu 610225, China

4 Sichuan University of Science and Engineering, Zigong 643000, China

1 Introduction

The tomographic gamma scanning (TGS) technique, a nondestructive assay, refers to a passive gamma analysis method. Both TGS and μ-medium radiographic imaging technologies are popular topics in the field of radiation detection imaging [1, 2]. The TGS technique was developed based on segmented gamma scanning (SGS) and was specifically developed to address the inability of the SGS technique to determine high- and medium-density non-uniformly distributed nuclear waste [3, 4]. Linear attenuation coefficient reconstruction is vital for TGS transmission measurement reconstruction. Reconstruction algorithms are primarily classified into two types. One type is an analytical reconstruction algorithm based on the Radon transform theory to directly and mathematically inversely calculate the image to be reconstructed; this type includes the filtered inverse projection algorithm (FBP) and the Radon inverse transform algorithm [5]. The second type

refers to an iterative reconstruction algorithm that converts the voxel and projection values of the reconstructed image into a series of linear equations and obtains the image to be reconstructed by solving the above linear equations; this type includes the algebraic iterative reconstruction algorithm and the statistical iterative reconstruction algorithm. Generally, algebraic iterative reconstruction algorithms involve algebraic reconstruction techniques (ART algorithms) and simultaneous iterative class reconstruction algorithms. Synchronous iterative class reconstruction algorithms include the simultaneous algebraic reconstruction technique (SART) and the diagonally relaxed orthogonal projection (DROP) algorithms [6]. Statistical iterative reconstruction algorithms include maximum likelihood expectation maximization (MLEM) and ordered subset expectation maximization (OSEM) algorithms [7]. Currently, the common TGS image reconstruction algorithms include the expectation–maximization (EM) algorithm and the ART algorithm [8, 9]. The EM algorithm is an iterative algorithm based on mathematical statistics that exhibits good operability and convergence, high noise immunity, and superior reconstructed image quality in a certain number of iterations; however, the convergence speed is too low [10]. Because of its large computation time and long reconstruction time, the ART algorithm spends most time on calculating the projection and inverse projection. The reconstruction efficiency of the ART algorithm has been improving for years by optimizing the algorithm and hardware acceleration, and it exhibits good noise immunity [11-13].

The two key factors for TGS transmission imaging are the solutions of the trial and projection matrices. Common methods adopted to calculate the trial matrix include the average method, Monte Carlo simulation, and computer graphics cropping. Specifically, the cropping method processes the defined graphics along the window boundary and displays them inside the window based on the preset window parameters. To offer clear and distinct objects for image identification and image processing, cropping seeks to remove all graphics from the image, except for the user-defined window. The cropping of line segments is a critical problem that must be solved in computer graphics. The four classical cropping algorithms that have been extensively used include the You-Dong Liang–Barsky algorithm in parametric form [14], the Nicholl–Lee–Nicholl algorithm based on region partitioning [15], the Cyrus-Beck algorithm for polygonal windows [16], and the Cohen-Sutherland algorithm based on region coding [17]. The You-Dong Liang–Barsky algorithm employs a parametric representation of the line segment to simplify the calculation of the coordinates of the intersection point between the location of the line segment and the border line of the rectangular cropping window to calculate the parameter value corresponding to the intersection point. Subsequently, the valid intersection point is determined by comparing the parameters of the intersection point with the parameter definition interval of the line segment being cropped to obtain the part of the line segment that should be retained after cropping. The Nicholl-Lee algorithm follows the coding algorithm to decrease the number of intersection-point calculations by adding more regional tests. The Cyrus-Beck algorithm is an early cropping algorithm proposed to deal with convex polygon cropping windows. For concave polygons, there is no general algorithm, whereas the method of splitting concave polygons into convex polygons has typically been adopted (e.g., extension line splitting and rotation splitting). In this study, an optimized Cohen-Sutherland algorithm is proposed based on the judgment of the vertical foot vector, which can effectively avoid the defects caused by the original algorithm (e.g., cutting invalid intersection points and significantly increasing the efficiency of solving the trace matrix).

2 Model construction and scanning

The TGS transmission measurement system is primarily adopted to quantitatively measure the content of radioactive material in nonuniform medium solid nuclear waste or nuclear waste drums, while obtaining the attenuation coefficient and activity distribution of radioactive material in nuclear waste drums [18]. To acquire more accurate reconstruction information, the samples measured in the nuclear waste drums were tested in equally spaced layers. Moreover, it is imperative to ensure that the same transmission scanning mode is employed for the respective layers of the material to be measured, and that the projection data, system matrix acquisition, and image reconstruction algorithm are all the same. On this basis, the linear attenuation coefficient and activity of the radioactive source in the drums were calculated. The TGS transmission measurement system comprises a radioactive source collimator, a nuclear waste drum, a detector shield, and an HPGe detector, and the scanning device is illustrated in Fig. 1.

A P-type HPGe coaxial GEM20P4-70 detector was used for the simulation in this study; its internal structure is shown in Fig. 2.

A P-type coaxial GEM20P4-70 detector was designed to detect high-energy charged particles and generate signals. It consists of a P-type silicon chip, a coaxial GEM, and a 70 μm thick detection layer. The silicon chip provides support and an interface, the coaxial GEM amplifies electrons to enhance the signal intensity and resolution, and the detection layer detects the energy deposition of charged particles. A cylindrical lead material served as a

Fig. 1 Model of TGS transmission measurement system
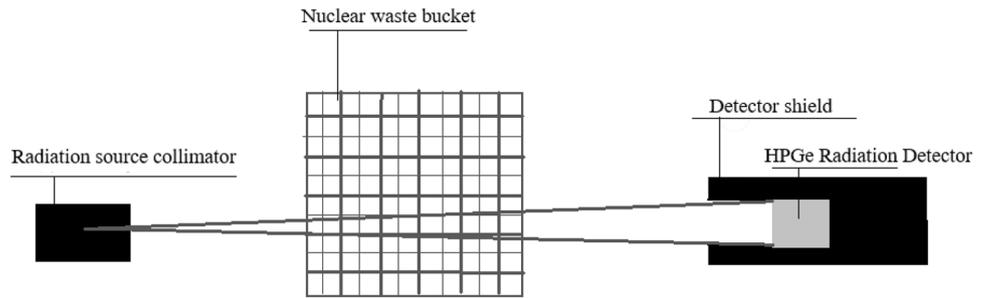
Fig. 2 Internal structure diagram of the HPGe detector

A = 52.7 mm	K: 0.8-mm Al
Crystal Diameter	L: 1-mm Al
B = 51.4 mm	M: 0.7-mm Ge/Li
Crystal Length	DEAD LAYER
C = 9.5 mm	N: 0.3-micron Ge/B
Hole Diameter	DEAD LAYER
D = 38.9 mm	
Hole Depth	

E: NOMINAL 5-mm RADIUS
F: 94-mm CUP LENGTH
G: 3-mm SPACE
H: 0.03-mm/0.03-mm Al/Mylar
I: 1-mm Al
J: NOMINAL 8-mm RADIUS
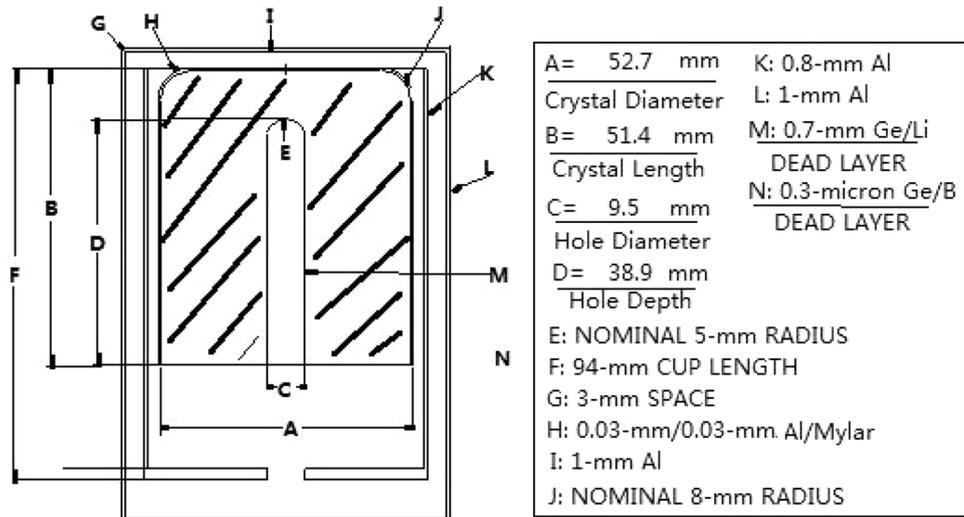
collimator to reduce the background. The centers of the detector probe, voxel center of the sample model, and the center of the transmission source were maintained on the same line during the measurement. The physical model of the TGS transmission measurement system was simplified, and an idealized "tensor" model was established, i.e., the transmission source was considered a point source and was located at the center of the sample voxel, and the beam had a certain width. The transmission source was a common ^{137}Cs point source, and the experimental source for simulation was a ^{60}Co point source, with energies of 0.661 MeV, 1.17 MeV and 1.33 MeV, respectively. Based on the actual levels of low and medium radioactive solid waste container steel boxes used in China [19], a voxel model of the sample nuclear waste square barrel was built with 25 voxels per layer, and the size of the respective voxel was 12 cm×12 cm×12 cm. To acquire sufficient measurement data, voxel information was collected maximally by examining different positions and angles during the respective layer scans. In addition, TGS transmission measurements were performed using three scanning methods (step, rotational, and vertical scans) in combination with layer-by-layer scanning to obtain the medium-filled material of the sample model. Before
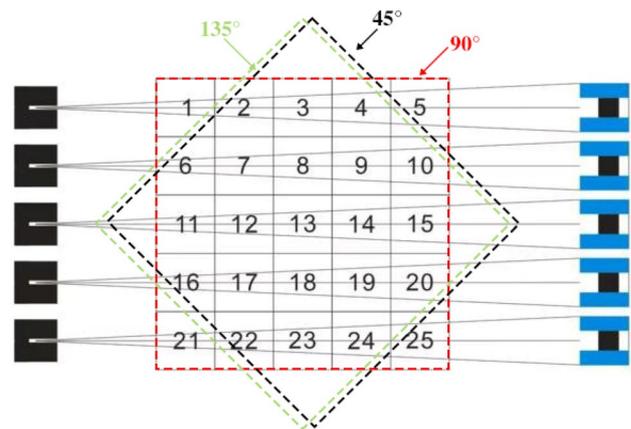
Fig. 3 (Color online) Schematic diagram of transmission scan measurement with a rotation angle

each scan, it was confirmed that the transmission source was in the same straight line as the detector and that the transmission source was placed outside the packaging body. The transmission source was also selected using a cylindrical collimator such that it could emit rays at a small solid angle. Figure 3 shows the scanning test

diagrams of the simulated transmission experiments with the medium to be tested rotated by 0°, 45°, 90°, and 135°.

The scanning measurement process is as follows:

1. Five equally spaced measurement points were selected, and the average value was taken as the measurement value by performing three measurements at the respective measurement positions, after which the projection data were calculated.
2. After the horizontal measurement was completed, the sample model of the packaging body was rotated clockwise with its geometric center as a circle, and the rotation angles were 0°, 45°, 90°, and 135°. In the same step as above, five equally spaced measurement points were selected at the respective rotation angles, and the average value was examined three times at the respective measurement position. Next, the projection data were calculated.
3. After all the scans were completed, the scale of one layer was completed, and the above operation was repeated to finish scanning all the sample models to acquire the scanned data. Although each layer was relatively independent, the calculation method for each layer was the same, such that only the measurement results of any one layer would be considered for simulation verification.

2.1 Mass attenuation coefficient reconstruction

Based on the attenuation law of rays in matter (i.e., the Lambert–Beer law) [20], the attenuation law in complex mixed non-homogeneous materials can be expressed as

$$\mu_m = \sum_{i=1}^{n} \mu_{mi} c_i, \tag{1}$$

where n indicates that there are n materials among them, μ_{mi} represents the linear attenuation coefficient of the ith material, and c_i represents the weight percentage of the ith material in the mixed material.

When the γ-rays are attenuated after entering the material, the transmittance is expressed as

$$S_i = C_i / C_{i_0}, \tag{2}$$

S_i is the transmittance of photons at the ith measurement position [21], C_i represents the count rate of photons after the detector has undergone attenuation at the ith measurement position after the rays have passed through the sample model, and C_{i0} is the count rate of photons measured by the detector at the ith position that have not undergone an attenuated matte. P_i is defined as the projected data at the ith measurement position.

$$P_i = \left| \ln(S_i) \right| \tag{3}$$

$$P_i = \sum_{i=1}^{n} \mu_i x_i \tag{4}$$

$$A_i = B_i \times S_i \tag{5}$$

The equations for the respective measurement points are derived from the decay law. On this basis, the measurement equation of the ith layer is obtained, where x_i denotes the trace matrix of the rays of the ith layer, A_i represents the matrix of the projection data of the ith layer, B_i represents the matrix of the decay coefficients of the ith layer. Furthermore, if S_i is a square matrix, a unique solution to Eq. (5) is obtained as:

$$B_i = A_i / S_i. \tag{6}$$

The first layer of the established voxel model was scanned to obtain 20 sets of count rates, and the obtained count vector was recorded as I^k. To calculate the transmittance, the sample package was removed and measured three times, and the average count rate was taken as the initial count of the radioactive source I_0. Then, according to Eq. (2), the projection data vector can be obtained as follows (7):

$$I^k = \left(I_1^k, I_2^k, I_3^k, \ldots, I_{20}^k \right)^{\mathrm{T}} \tag{7}$$

$$P^k = \left(\left| \ln\left(\frac{I_1^k}{I_0} \right) \right|, \left| \ln\left(\frac{I_2^k}{I_0} \right) \right|, \left| \ln\left(\frac{I_3^k}{I_0} \right) \right|, \ldots, \left| \ln\left(\frac{I_{20}^k}{I_0} \right) \right| \right)^{\mathrm{T}} \tag{8}$$

We then solved the attenuation coefficients according to Eq. (6). Twenty sets of linear equations were established based on the scan results. The attenuation coefficients were calculated using Eq. (6) using 20 sets of linear equations.

2.2 Cohen-Sutherland coding cropping algorithm and its improvement

The Cohen-Sutherland clipping algorithm was one of the earliest and most widely used clipping algorithms. The basic concept is to first use the area code to identify the location of the end of a line segment. The specific position of the line segment is identified based on the code. Line segments that are not all inside or outside the window must find their intersection with the window. The part outside the window I discarded, and the rest are judged as a new line segment. After the two clipping judgments, it was possible to determine whether the line segment should be partially or completely cut. Because the Cohen-Sutherland algorithm cannot effectively judge whether a line segment is outside
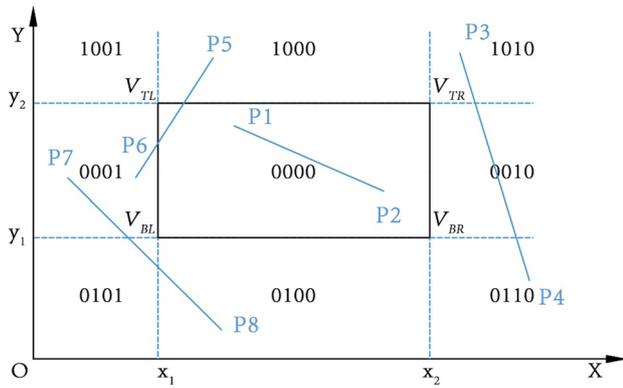
Fig. 4 Schematic diagram of Cohen-Sutherland cropping algorithm region segmentation
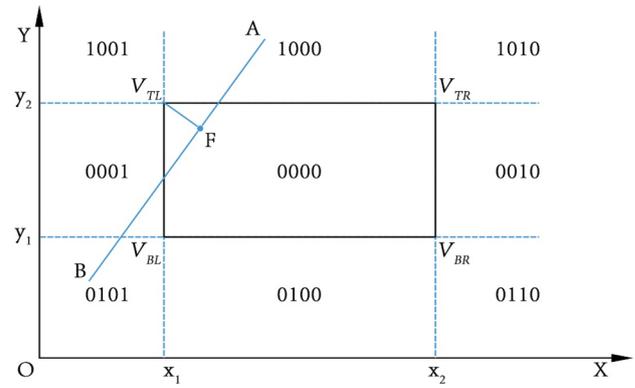
Fig. 5 V_{TL} line segment dip foot

the window, which greatly reduces computational efficiency, an improved scheme is proposed.

The Cohen-Sutherland algorithm uses the four edges of the rectangular cropping window to divide the two-dimensional plane into nine regions, which are marked with the 4-bit binary code $C_tC_bC_rC_1$, as shown in Fig. 4. The basic idea of the algorithm is as follows: The codes of the two ends of the straight-line segment to be cropped are recorded as code1 and code2, respectively, and there are three cases with the window:

1. When code1 = code2 = 0 (P1P2), it is completely visible and is considered.
2. When code1 & code2 ≠ 0 (P3P4) (& is a bit and operation), it is not visible at all and is discarded.
3. When the "take" or "discard" condition is not met, the line segment is divided into two segments at the intersection with the window boundary, one of which is completely outside the window and discarded; then, the above process is repeated for the other segment.

The advantage of the Cohen-Sutherland trimming algorithm is that the first and second cases can be separated without performing intersection operations. However, the third case is computationally intensive. As depicted in the figure, line segment P7P8 does not satisfy the above two cases, and according to the original algorithm, the intersection operation must be performed. In contrast, line segment P7P8 is outside the window. Thus, it is meaningless to intersect it. To address this problem, the algorithm was further optimized, as shown in Fig. 5. The respective endpoint of the window forms a vertical line to the line segment and determines whether foot x is within the window. A line segment is considered to have passed through the window which allows the intersection operation if there are one or more intersection points. If there are fewer intersection points, the line segment is considered to be

outside the window and is immediately discarded with no further processing.

Let the coordinates of the two endpoints of any line AB be (x_a, y_a), (x_b, y_b), and the coordinates of the four vertices of the window are (x_1, y_1), (x_1, y_2), (x_2, y_1), and (x_2, y_2), and the coordinates of the vertical foot F are (x_f, y_f).

V_{TL} to line segment drape.

$$\overrightarrow{V_{TL}F} = \left(x_f - x_1, y_f - y_2\right) \tag{9}$$

$$\overrightarrow{AB} = \left(x_b - x_a, y_b - y_a\right) \tag{10}$$

$$\overrightarrow{AF} = \left(x_f - x_a, y_f - y_a\right) \tag{11}$$

From the vector-perpendicular relationship, it follows that

$$\overrightarrow{V_{TL}F} \perp \overrightarrow{AB} \tag{12}$$

Thus, it can be obtained that

$$\left(x_f - x_1\right)\left(x_b - x_a\right) + \left(y_f - y_2\right)\left(y_b - y_a\right) = 0 \tag{13}$$

The vertical foot F is located on line segment AB, which is known from vector collinearity.

$$\overrightarrow{AF} = K\overrightarrow{AB} \tag{14}$$

$$\left(x_f - x_a\right) = k\left(x_b - x_a\right) \tag{15}$$

$$\left(y_f - y_a\right) = k\left(y_b - y_a\right) \tag{16}$$

Substituting the equation gives:

$$k = -\frac{\left(x_a - x_1\right)\left(x_b - x_a\right) + \left(y_a - y_2\right)\left(y_b - y_a\right)}{\left(x_b - x_a\right)^2 + \left(y_b - y_a\right)^2} \tag{17}$$

Then, the coordinates of the vertical foot of V_{TL} are

$$x_{f\mathrm{TL}} = -\frac{(x_a - x_1)(x_b - x_a) + (y_a - y_2)(y_b - y_a)}{(x_b - x_a)^2 + (y_b - y_a)^2}(x_b - x_a) + x_a$$

(18)

$$y_{f\mathrm{TL}} = -\frac{(x_a - x_1)(x_b - x_a) + (y_a - y_2)(y_b - y_a)}{(x_b - x_a)^2 + (y_b - y_a)^2}(y_b - y_a) + y_a$$

(19)

If the pendant foot is inside the window, then

$$x_1 \leq x_{f\mathrm{TL}} \leq x_2$$

(20)

Similarly, the coordinates of the perpendiculars of the remaining vertices of the window to any line segment are

$$y_1 \leq y_{f\mathrm{TL}} \leq y_2$$

(21)

V_{BL} to the perpendicular line of the line segment is

$$x_{f\mathrm{BL}} = -\frac{(x_a - x_1)(x_b - x_a) + (y_a - y_1)(y_b - y_a)}{(x_b - x_a)^2 + (y_b - y_a)^2}(x_b - x_a) + x_a$$

(22)

$$y_{f\mathrm{BL}} = -\frac{(x_a - x_1)(x_b - x_a) + (y_a - y_1)(y_b - y_a)}{(x_b - x_a)^2 + (y_b - y_a)^2}(y_b - y_a) + y_a$$

(23)

V_{TR} to the perpendicular line of the line segment is

$$x_{f\mathrm{TR}} = -\frac{(x_a - x_2)(x_b - x_a) + (y_a - y_2)(y_b - y_a)}{(x_b - x_a)^2 + (y_b - y_a)^2}(x_b - x_a) + x_a$$

(24)

$$y_{f\mathrm{TR}} = -\frac{(x_a - x_2)(x_b - x_a) + (y_a - y_2)(y_b - y_a)}{(x_b - x_a)^2 + (y_b - y_a)^2}(y_b - y_a) + y_a$$

(25)

V_{BR} to the line segment vertical foot is

$$x_{f\mathrm{BR}} = -\frac{(x_a - x_2)(x_b - x_a) + (y_a - y_1)(y_b - y_a)}{(x_b - x_a)^2 + (y_b - y_a)^2}(x_b - x_a) + x_a$$

(26)

$$y_{f\mathrm{BR}} = -\frac{(x_a - x_2)(x_b - x_a) + (y_a - y_1)(y_b - y_a)}{(x_b - x_a)^2 + (y_b - y_a)^2}(y_b - y_a) + y_a$$

(27)

If the coordinates of the foot are within the window (x_1, x_2), (y_1, y_2), the line passes through the window. The specific flowchart is shown in Fig. 6.

According to the TGS model, because the "tensor" model is between the source and the detector, the range path of γ-rays is nearly straight, and the effective line segments in the cropping area are summed up and averaged to approximate the length of the trajectory of γ-rays through the voxel, i.e., $L = \frac{\sum_{n=1}^{n} L_n}{n}$, the resulting visuals of cropping 2 and 10 line segments are shown in Fig. 7 [12].

To test the cropping efficiency of the two algorithms, experiments were conducted on a Windows 10 computer configured with an AMD Ryzen 32300U processor at 2.0 GHz with four cores and eight threads. The control variable method was adopted to ensure that both algorithms were performed under the same conditions, and the experimental results showed that both algorithms obtained the same trail matrix when performing voxel segmentation on square nuclear waste buckets; however, the cropping times were different, as shown in Table 1.

As indicated by the running time data in Table 1, the improved Cohen−Sutherland algorithm runs faster than the original algorithm in cutting voxel split line segments because the original algorithm cannot effectively judge whether the line segments are outside the window in the cutting area and will repeat the judgment of invalid intersection points by introducing the judgment of the vertical foot vector, thereby avoiding the calculation of invalid intersection points. This significantly shortens the cropping time and improve the computational efficiency.

2.3 OSEM algorithm

The ordered subset (OS) algorithm is also a common acceleration algorithm used in numerical computation [22]. The OS algorithm was proposed by Hudson et al. to address the problems of low computational efficiency and slow convergence in the statistical iterative reconstruction of CT images. The OS algorithm divides the projection data into n subsets by arranging them, and the above subsets of projection data are also called ordered subsets. The level of the subset (OS level) is determined by the number of subset divisions n. The reconstruction of an image using the OS algorithm refers to a process in which the reconstructed image is continuously corrected, and the reconstructed image is updated a total of *n* times. As the OS algorithm adopts projection data inside each ordered subset, it can realize the alignment of each pixel of the image once, and the reconstructed image is updated once as a result. However, because the projection data comprise n ordered subsets, the OS algorithm should correct each pixel n times, and the reconstructed image is updated n times accordingly.

The OSEM algorithm, also known as the ordered subset maximum expectation algorithm, is an application of the OS method to EM algorithms. Each iteration of the EM algorithm consists of two steps (i.e., the E step and the M step), where the E step determines the expectation and the M step determines the maximum. In the EM algorithm, the correction value of the image is obtained using all the projection values. Additionally, in the OSEM algorithm, the correction value of the image is determined from the projection data within the respective subset. OSEM applies the EM algorithm to each subset of the
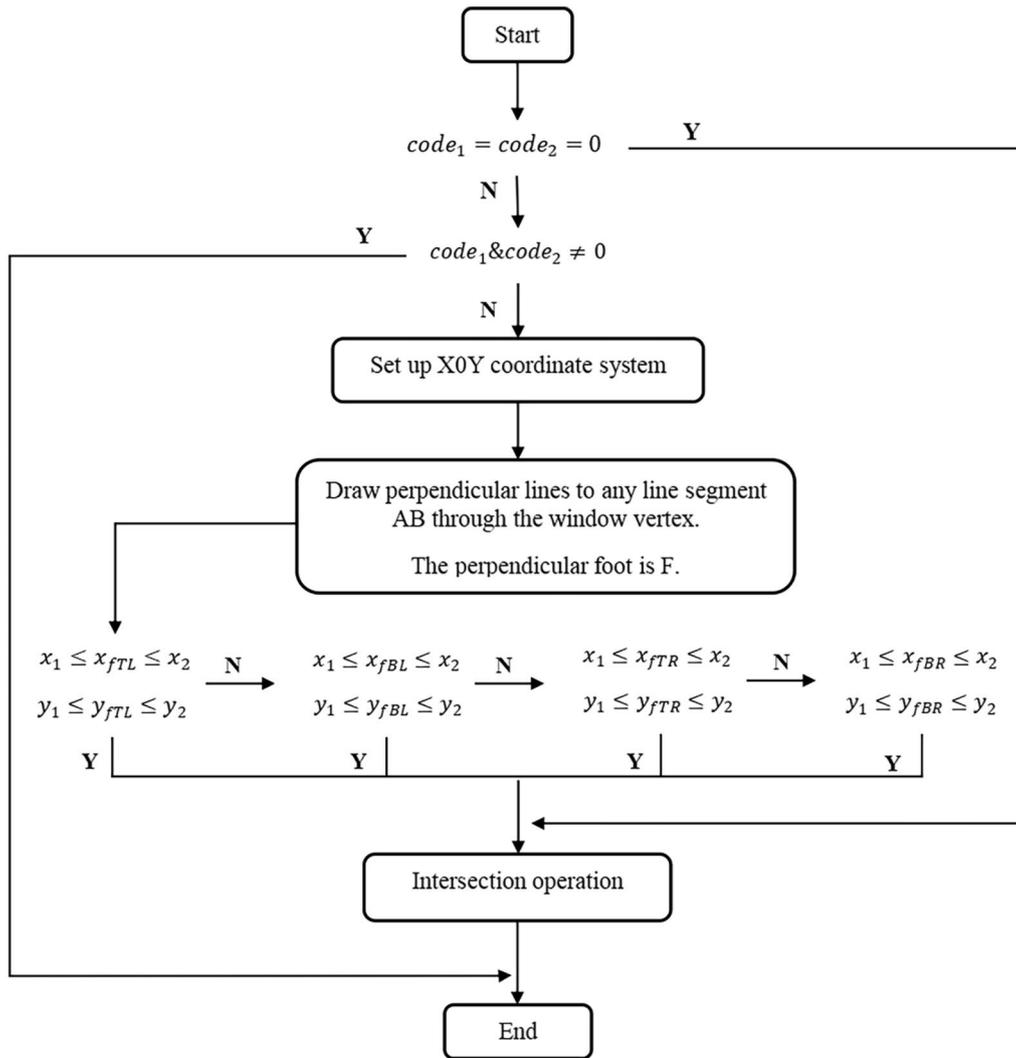
Fig. 6 Cohen-Sutherland cropping algorithm-specific flowchart

projection data. In the OSEM algorithm, the projection matrix is divided into n ordered subsets $\{S_1, S_1, \ldots, S_T\}$, the standard EM algorithm is adopted to maximize the likelihood function for each subset of the projected data in turn, and the reconstructed subset serves as the initial value for the next subset. Similar to the OS algorithm, the OSEM algorithm reconstructs an image with iterative correction updates, and the image is updated n times. When the OSEM algorithm completes the correction of the pixel points using the nth subset of the projection data, the first iteration is completed, and the reconstruction result serves as the initial value for the next iteration. However, unlike the OS algorithm, the OSEM algorithm adds the maximum likelihood function of the previous subset to the next subset and participates as the initial value of the next subset. Thus, the correlation between the reconstructed images increases.

$$x_j^{(k+1)} = \frac{\sum_{i \in S_n} \frac{a_{ij} p_i}{\sum_l a_{ij} x_l^{(k)}}}{\sum_{i \in S_n} a_{ij}} x_l^{(k)} \tag{28}$$

In the OSEM algorithm, data subsets are typically divided in terms of projection angles, and the OSEM algorithm tends to distribute the projected data into ordered subsets according to the symmetric balance principle to guarantee that the pixels contribute approximately equally to each subset.

The specific steps of the OSEM algorithm are as follows:

Assign an initial value to the unknown quantity

$$x_j^{(k)} = x_j^{(0)}, \ j = 1, 2, \ldots, J, \ k = 1. \tag{29}$$

For the nth subset,

Estimate all projections within the subset as
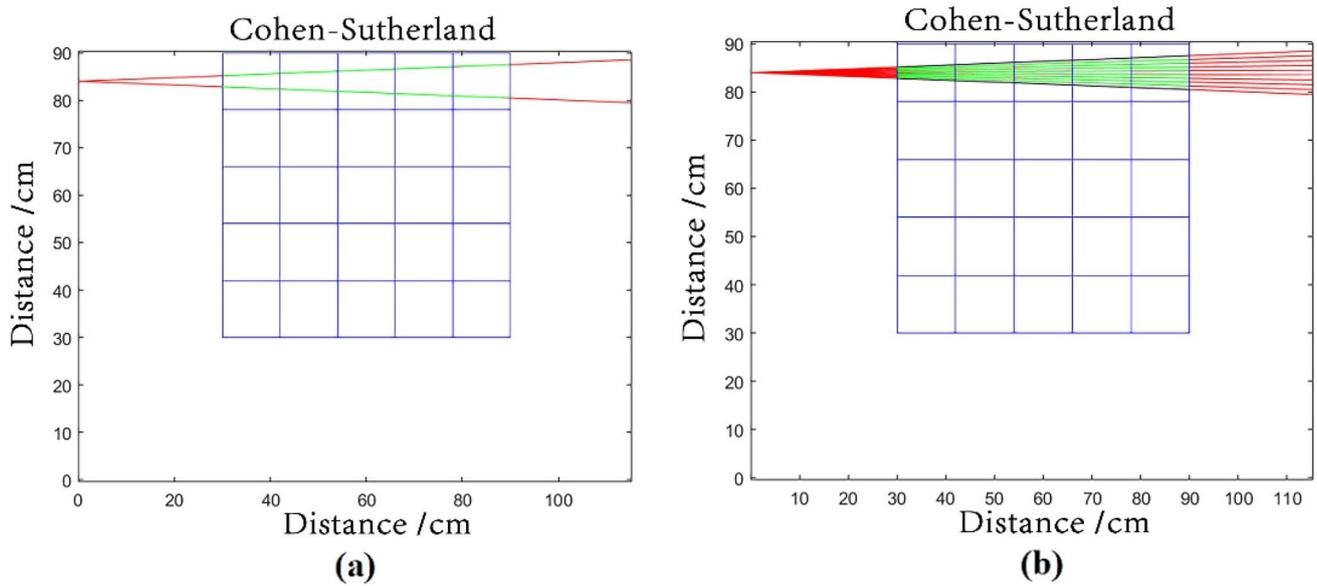
Fig. 7 (Color online) **a** The effect of cutting 2 strips; **b** The effect of cutting 10 strips

Table 1 Comparison of the running time of the original algorithm and the improved Cohen-Sutherland algorithm

No	Number of cropping codes (entries)	Running time of the original algorithm (s)	Running time of the improved algorithm (s)
1	2	0.3787	0.3129
2	10	0.3709	0.2708
3	20	0.3642	0.2368
4	50	3.6050	3.2658

$$\bar{p}_i = \sum_{i=1}^{J} a_{ij} x_j^{(k)}, \ i \in S_n. \tag{30}$$

Calculate the error as

$$\Delta_i = \frac{p_i}{\bar{p}_i}, \ \ i \in S_n. \tag{31}$$

Calculate the correction value of the jth unknown quantity as

$$C_j = \frac{1}{\sum_{i=1}^{I} a_{ij}} \sum_{i=1}^{I} \Delta_i a_{ij}. \tag{32}$$

Correct the values of x_j and $x_j^{(k+1)} = x_j^{(k)} \times C_j$; here, we correct them with all rays that pass through the voxel in the subset.

Repeat operation (2) until n subsets of operations are completed, and one round of iteration is completed. $k = k+1$: Repeat operations (2) and (3) with the result of the previous

iteration as the initial value and perform a new round of iterations until a result that meets the convergence requirement is obtained.

The subset level of the OSEM algorithm has a vital effect in terms of the effect of the reconstructed image. When a high subset level of the OSEM algorithm is selected, the reconstructed images converge rapidly. However, as the number of iterations tends to increase, it will lead to undesirable noise levels occur in image regions with low activity, and the reconstructed image appears divergent. When a low subset level is selected, the reconstructed image converges to a low value, and it preferentially recovers low-frequency element information and loses high-frequency information [23]. In the absence of noise, the convergence speed of the image is proportional to the subset segmentation size. Accordingly, if the OSEM algorithm is employed for reconstruction, choosing a smaller number of segmentation subsets not only requires more time for iteration but may also lack some high-frequency information about the image in the process; however, if a larger number of segmentation subsets is chosen, the image will be scattered in the iterative process. Therefore, different subset levels can significantly affect the convergence speed of the reconstructed images and the quality of the reconstructed images.

The length of the respective voxel in the square barrel is rapidly cropped by the code-cropping algorithm based on the vertical foot vector judgment proposed above, thus providing the path length matrix of the rays in the respective voxel; then, the attenuation coefficients of each layer in the barrel at the transmitted energy are reconstructed using the OSEM algorithm. To verify the accuracy of the OSEM algorithm,

two experimental models were selected: a single medium model of mixed soil and polyethylene and the concrete, polyethylene, and aluminum mixture model. The first layer of the square barrel sample model was selected as the object of study, and voxels 7, 8, 12, and 13, shown in Fig. 8a, were filled with concrete and polyethylene successively; voxels 2, 8, 9, 13, 14, 17, and 22, as shown in Fig. 8b, were filled with polyethylene, concrete, and aluminum successively, while the other voxels were filled with air. The reference values of the attenuation coefficients of the three media at different transmission energies are listed in Table 2.

3 Evaluation and results analysis

To objectively and accurately verify the effectiveness of the computer-based graphic cropping algorithm, three image quality evaluation parameters, i.e., relative mean deviation (RMD), root-mean-square error (RMSE), and Pearson correlation coefficient (PCC), were introduced to evaluate the accuracy of the reconstructed values of all 25 voxels in the square barrel based on the known true distribution of the samples to be tested and their material attenuation coefficient reference values.

RMSE is the square root of the ratio of the square of the deviation of the predicted value from the true value to the number of observations N. It was adopted to measure the degree of deviation between the observed and true values; the smaller the RMSE, the closer the predicted value was to the reference value, that is, the higher the accuracy. The RMSE is written as

$$X_{\mathrm{rms}} = \sqrt{\frac{\sum_{i=1}^{n} X_i^2}{N}}, \tag{33}$$

where X_i represents the difference between the corresponding OSEM algorithm-reconstructed value and the reference

Table 2 Reference values of the attenuation coefficient of dielectric materials under different transmission characteristic energy values

Media materials	Density (g/cm^3)	Attenuation coefficient reference value (cm^{-1})		
		0.661 MeV	1.17 MeV	1.33 MeV
Concrete	2.3	0.178	0.136	0.127
Polyethylene	0.93	0.072	0.055	0.051
Aluminum	2.7	0.201	0.153	0.143

value in the ith case, and N denotes the N cases of that unique identical variable under the unique identical variable.

The PCC is the quotient of the covariance and standard deviation between X and Y. This parameter was adopted to measure the magnitude of the correlation between two variables. Its value range is [–1,1]; a value of 1 indicates that the two random variables have a positive correlation, a value of –1 reveals a completely negative correlation between the two random variables, and a value of 0 represents no linear correlation between the two random variables. The calculation is as follows:

$$\gamma = \frac{\sum_{i=1}^{n} (X_i - \overline{X})(Y_i - \overline{Y})}{\sqrt{\sum_{i=1}^{n} (X_i - \overline{X})^2 \sum_{i=1}^{n} (Y_i - \overline{Y})^2}}, \tag{34}$$

where n denotes the number of preset voxels, X_i represents the computed value obtained in the ith case using the encoding algorithm, and Y_i expresses the reconstructed value obtained in the ith case using the OSEM algorithm. $\overline{X}, \overline{Y}$ represent the corresponding reference values. The Pearson phase relationship quantifies the numerical correlation between the reconstructed image and the real image as well as the reconstruction similarity; the closer its value is to 1, the closer the reconstructed image will be to the real image, consistent with its higher reconstruction quality.

Fig. 8 a Single dielectric material preset model. **b** Mixed material preset model

(a)

(b)
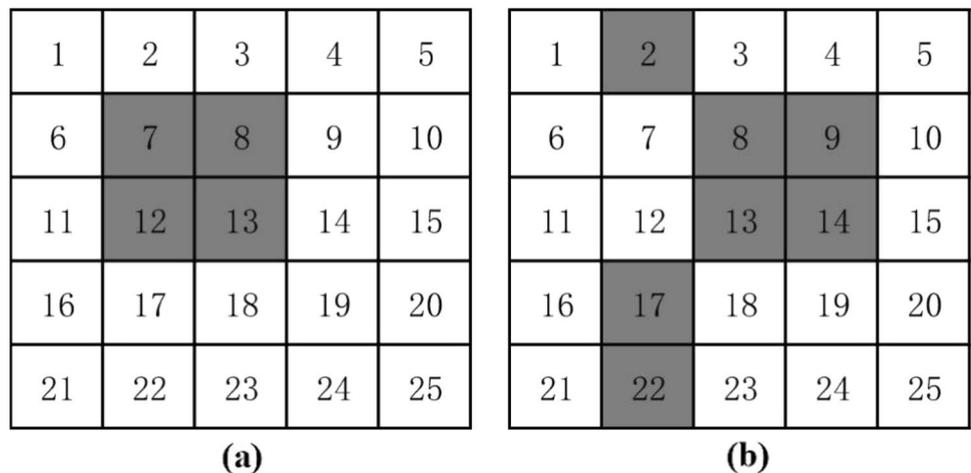
In this study, two transmission sources, ^{137}Cs and ^{60}Co, were adopted: the first model was preset with two materials (including concrete and polyethylene) in voxels 7, 8, 12, and 13 in the square barrel, and the second model was filled with a mixture of polyethylene, cement, and aluminum in voxels 2, 8, 9, 13, 14, 17, and 22. Subsequently, a coding cropping algorithm based on the draped foot vector judgment was adopted after calculating the trial matrix of the respective voxel. The OSEM algorithm was used to determine the reconstruction values of the attenuation coefficients when the cropped line segments in the voxels were 2, 12, 100, and

1000. The resulting transmission-reconstructed images are shown in Fig. 9.

The relationships of the PCC, RMSE, and RMD with an increasing number of cut lines for the high-density medium concrete material, low-density medium polyethylene material, and mixed materials at transmission energies of 0.661, 1.17, and 1.33 MeV, respectively, are shown in Table 3.

As shown in Table 3, when the preset material in the square barrel is high-density concrete with a single medium material, the RMD and RMSE between the reconstructed
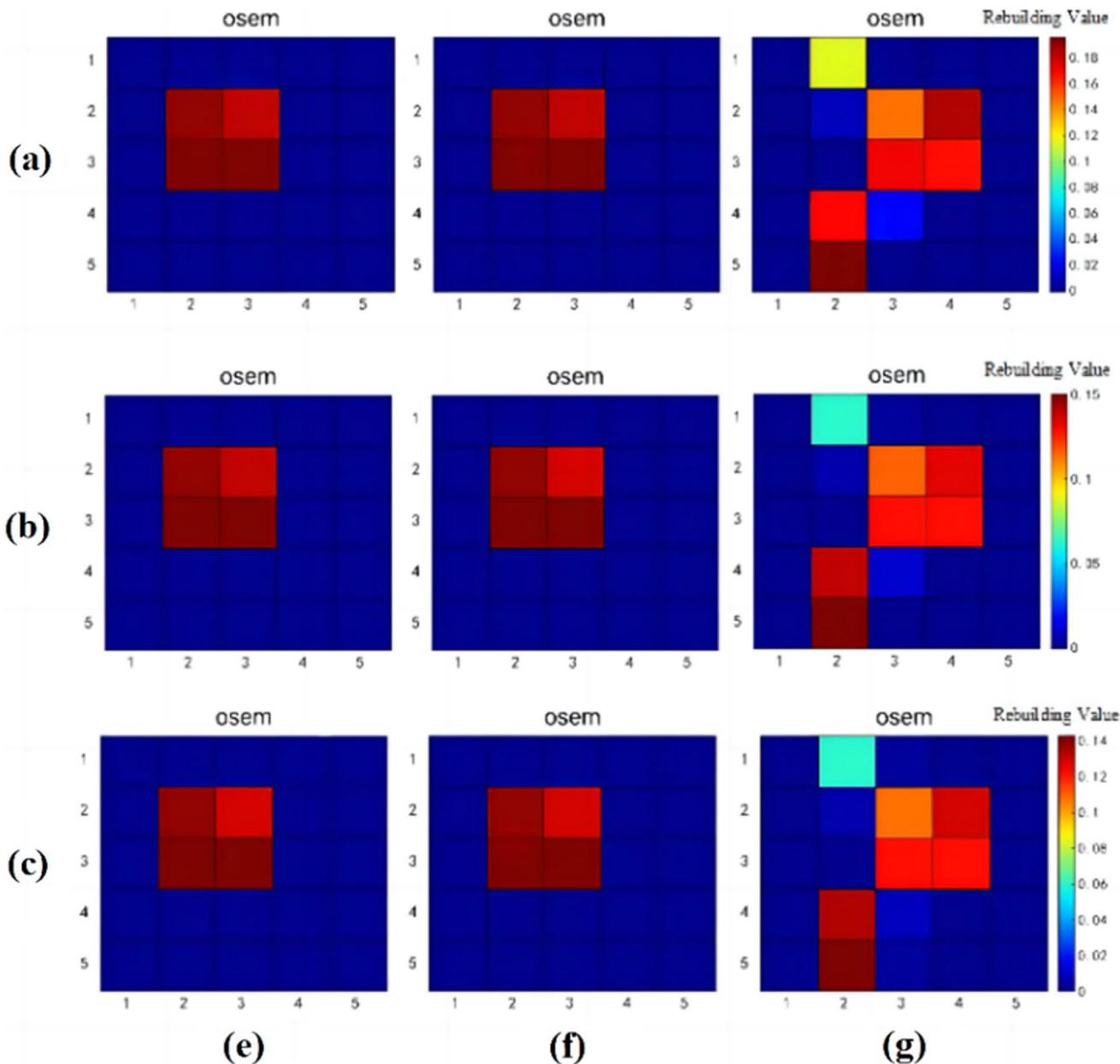
Fig. 9 (Color online) Transmission and reconstruction images of three models (**e**) concrete (**f**) polyethylene (**g**) mixture at different characteristic energies **a** 0.661 MeV **b** 1.17 MeV **c** 1.33 MeV

Table 3 Evaluation parameter performance of three different dielectric materials at different energies

Transmission energy (MeV)	Material	Number of cuts	PCC	RMSE	RMD
0.661	Concrete	2	0.8660	0.0082	0.0357
		12	0.9442	0.0060	0.0250
		100	0.9350	0.0059	0.0244
		1000	0.9338	0.0059	0.0243
	Polyethylene	2	0.8496	0.0108	0.1406
		12	0.9460	0.0097	0.1302
		100	0.9416	0.0097	0.1294
		1000	0.9412	0.0097	0.1293
	Mixture	2	0.9064	0.0218	0.136
		12	0.8755	0.0233	0.1618
		100	0.8708	0.0235	0.1641
		1000	0.8703	0.0235	0.1643
1.17	Concrete	2	0.8608	0.0073	0.0442
		12	0.9764	0.0063	0.0339
		100	0.9771	0.0063	0.0346
		1000	0.9771	0.0063	0.0346
	Polyethylene	2	0.8627	0.0074	0.1218
		12	0.9771	0.0065	0.1111
		100	0.9789	0.0064	0.1103
		1000	0.9790	0.0064	0.1102
	Mixture	2	0.9766	0.0083	0.0711
		12	0.9708	0.0097	0.0879
		100	0.9697	0.0099	0.0896
		1000	0.9696	0.0099	0.0898
1.33	Concrete	2	0.8526	0.0066	0.0385
		12	0.9753	0.0049	0.0246
		100	0.9788	0.0048	0.0240
		1000	0.9791	0.0048	0.0239
	Polyethylene	2	0.8619	0.0082	0.1534
		12	0.9399	0.0075	0.1431
		100	0.9315	0.0075	0.1423
		1000	0.9305	0.0075	0.1422
	Mixture	2	0.9727	0.0075	0.0589
		12	0.9702	0.0083	0.0798
		100	0.9693	0.0085	0.0815
		1000	0.9692	0.0085	0.0818

attenuation coefficient and the standard reference value tend to decrease with an increase in the cut line segments in the respective voxels, and the PCC tends to converge to 1. When the preset material in the square barrel is polyethylene with a low single medium density, with an increase in the cut line segment, the reconstructed attenuation coefficient and the reference standard value have the same variation trend for the three evaluation parameters with the high-density medium, whereas the image evaluation quality index is worse than that of the high-density medium. When there are multiple preset materials in the square barrel, with an increase in the number of cut strips, the interaction between different media materials, owing to their different densities and attenuation coefficients, will lead to poorer quality indicators for all three image evaluations. As revealed by this result, the accuracy of the image reconstruction was poor when the preset materials were more complex. A possible reason for this is the mutual scattering effect caused by the rays passing through each material. Furthermore, the attenuation coefficients of both preset models show a stable trend after 100 line segments are cut in the voxel, indicating that the average value can be approximated instead of the path length of γ-rays through the voxel when more line segments are cut in the voxel.

4 Conclusion

Using TGS technology, this study proposes an encoding and clipping method based on perpendicular vector judgment that can quickly calculate the voxel trajectory length of nuclear waste packaging. The results demonstrate that the improved coding clipping technique may significantly increase the clipping speed by clipping multiple line segments within sample voxels. The RMD, RMSE, and PCC were used as the three parameters for image evaluation. As the number of line segments clipped within each voxel increased, the accuracy of the attenuation coefficient in image reconstruction gradually improved. High-density materials exhibited better performances than low-density materials for all image reconstruction metrics. The reconstructed attenuation coefficients tended to stabilize when more than 100 line segments were cut within a voxel. The path length of the gamma rays passing through the voxel can be roughly estimated using the average value. Only the first-layer scan data of the validation sample model were used for verification because of the small number of sample voxels, sparse voxel grid partitioning, simple preset materials employed in the project simulation, and insufficient energy of the transmitted source. Moreover, the results were not supported by relevant experimental data. Therefore, by addressing these constraints in future studies, we can further improve and refine our simulations.

Declarations

Conflict of interest The authors declare that they have no competing interests.

References

1. X.T. Ji, S.Y. Luo, Y.H. Huang et al., A novel 4D resolution imaging method for low and medium atomic number objects at the centimeter scale by coincidence detection technique of cosmic-ray muon and its secondary particles. Nucl. Sci. Tech. **33**, 2 (2022). https://doi.org/10.1007/s41365-022-00989-0
2. Y.P. Cheng, R. Han, Z.W. Li et al., Imaging internal density structure of the Laoheishan volcanic cone with cosmic ray muon radiography. Nucl. Sci. Tech. **33**, 88 (2022). https://doi.org/10.1007/s41365-022-01072-4
3. L. Li, Study on the Transmission and emission reconstruction techniques for tomographic gamma scanner in drummed nuclear waste. Chengdu University of Technology (2015) (**in Chinese**)
4. R.J. Estep, T.H. Prettyman, G.A. Sheppard, Tomographic gamma scanning to assay heterogeneous radioactive waste. Nucl. Sci. Eng. **118**(3), 145–152 (1994). https://doi.org/10.13182/nse94-a19380
5. Q.H. Zhang, W.H. Hui, D. Wang et al., A novel algorithm for transmission image reconstruction of tomographic gamma scaners. Nucl. Sci. Tech. **21**, 177–181 (2010). https://doi.org/10.13538/j.1001-8042/nst.21.177-181
6. Y.C. Yan, M.Z. Liu, J.K. Xiong et al., An improved ART algorithm for attenuation coefficient reconstruction of tomographic gamma scanners. Nucl. Instrum. Methods Phys. Res. Sect. A **1038**, 166910 (2022). https://doi.org/10.1016/j.nima.2022.166910
7. J.W. Zhao, W.N. Su, An iterative image reconstruction algorithm for SPECT. Nucl. Sci. Tech. **25**, 030302 (2014). https://doi.org/10.13538/j.1001-8042/nst.25.030302
8. J. Kim, S. Jung, J. Moon et al., A feasibility study on gamma-ray tomography by Monte Carlo simulation for development of portable tomographic system. Appl. Radiat. Isotop. **70**(2), 404–414 (2012). https://doi.org/10.1016/j.apradiso.2011.09.019
9. A.J. He, X.G. Tuo, R. Shi et al., An improved OSEM iterative reconstruction algorithm for transmission tomographic gamma scanning. Appl. Radiat. Isotop. **142**, 51–55 (2018). https://doi.org/10.1016/j.apradiso.2018.09.001
10. Y. Tuaç, Y. Güney, O. Arslan, Parameter estimation of regression model with AR (p) error terms based on skew distributions with EM algorithm. Soft. Comput. **24**(5), 3309–3330 (2020). https://doi.org/10.1007/s00500-019-04089-x
11. A.M. El-Khatib, A.A. Thabet, M.A. Elzaher et al., Study on the effect of the self-attenuation coefficient on γ-ray detector efficiency calculated at low and high energy regions. Nucl. Eng. Technol. **46**(2), 217 (2014). https://doi.org/10.5516/NET.04.2013.077
12. M.S. Badawi, M.M. Gouda, S.S. Nafee et al., New algorithm for studying the effect of self attenuation factor on the efficiency of γ-rays detectors. Nucl. Instrum. Methods Phys. Res. Sect. A **696**, 164–170 (2012). https://doi.org/10.1016/j.nima.2012.08.089
13. M.S. Badawi, I. Ruskov, M.M. Gouda et al., A numerical approach to calculate the full-energy peak efficiency of HPGe well-type detectors using the effective solid angle ratio. J. Instrum. **9**, P07030 (2014). https://doi.org/10.1088/1748-0221/9/07/P07030
14. R. Andreev, E. Sofianska, New algorithm for two-dimensional line clipping. Comput. Graph. **15**, 519–526 (1991). https://doi.org/10.1016/0097-8493(91)90051-I
15. Y.D. Liang, B.A. Barsky, A new concept and method for line clipping. ACM **3**(1), 1–22 (1984). https://doi.org/10.1145/357332.357333
16. Q.H. Zhang, H.Z. Sui, F. Lu et al., Reconstruction methods of transmission image in tomographic gamma scanning. Atom. Energy Sci. Technol. **38**, 162–165 (2004). https://doi.org/10.3969/j.issn.1000-6931.2004.02.014. (**in Chinese**)
17. D. Hearn, M. Pauline Baker, *Computer graphics: C Version*, 2nd edn. Tsinghua University Press, Beijing, 2004. (**in Chinese**)
18. R. Venkataraman, M. Villani, S. Croft et al., An integrated Tomographic Gamma Scanning system for non-destructive assay of radioactive waste. Nucl. Instrum. Meth. Phys. Res. Sect. A **579**, 375–379 (2007). https://doi.org/10.1016/j.nima.2007.04.125
19. Nuclear industry standard of the People's Republic of China steel drums for low and medium level radioactive solid waste containers EJ 1042–2014.
20. A.J. He, Study on iterative reconstruction algorithm of transmission tomographic gamma scanning. Dissertation, Chengdu University of Technology (2019). https://doi.org/10.26986/d.cnki.gcdlc.2019.001031 (**in Chinese**)
21. C. Lu, W.G. Gu, N. Qian et al., Study of image reconstruction using dynamic grids in tomographic gamma scanning. Nucl. Sci. Tech. **23**, 277–283 (2012). https://doi.org/10.13538/j.1001-8042/nst.23.277-283
22. H.M. Hudson, R.S. Larkin, Accelerated image reconstruction using ordered subsets of projection data. IEEE Trans. Med. Imaging **13**(4), 601–609 (1994). https://doi.org/10.1109/42.36310810.16208/j.issn1000-7024.2015.09.040. (**in Chinese**)
23. J. Yang, M.Q. Wang, L. Shi et al., Research and comparison on OSEM and its improved reconstruction algorithms. Comput. Eng. Design **36**, 2524–2527 (2015)